ST-ECF Instrument Science Report ACS-2005-08

Updated Wavelength Calibration for the WFC/G800L grism

S. S. Larsen, J. R. Walsh, July 2005

ABSTRACT

A revised wavelength calibration is presented for the G800L grism used with the ACS Wide Field Channel. Combining existing calibration data with new observations of the Wolf-Rayet star WR96, we achieve improved coverage of the WFC field-of-view. Deviations from the previously published wavelength calibration are less than 1 pixel (40 Å) for the +1st order over nearly the entire field. The new wavelength calibration has been implemented into revised configuration files for the aXe spectral extraction software, available via the ST-ECF web site and it is recommended that these be used for future reductions of G800L/WFC slitless spectroscopy data.

Introduction

The Advanced Camera for Surveys (ACS) is equipped with several dispersing elements for slitless spectroscopy. The most frequently used of these is the G800L grism, which can be used both with the *high resolution channel* (HRC) and with the *wide field channel* (WFC). The G800L covers the wavelength range from about 5500 Å to 10000 Å with a dispersion of ~40 Å / pixel in the 1st order when used with the WFC. In addition to the G800L, the ACS *solar blind channel* (SBC) has two prisms (PR110L and PR130L) covering the wavelength range from ~1200 Å - 2000 Å. An additional prism (PR200L) covering the range from ~1800 Å - 4000 Å is mounted in the high resolution channel. This report provides an updated wavelength calibration for the G800L used with the WFC. The calibration of the G800L/HRC is described in ACS ISR-03-07 (Pasquali et al. 2003b).

An in-orbit wavelength calibration of the G800L/WFC has previously been presented in ISR-03-01 (Pasquali et al. 2003a), based on observations of two Wolf-Rayet stars acquired during the SMOV programme (WR45) and the INTERIM calibration programme (WR96). These calibrator targets and the criteria leading to their selection are described in Pasquali et al. (2003a). In the INTERIM programme (Prog. No. 9568), the star WR96 was observed at 5 positions across each of the WFC detectors, allowing a mapping of the significant spatial variations in the wavelength solution due to the geometric distortions in

ACS. Additional observations of WR96 with improved spatial coverage were obtained in Cycle 12 under programme 10058 and are used here (together with the earlier data) to verify and refine the existing G800L wavelength calibration. A planetary nebula (LMC-SMP-81) was also observed during the Cycle 12 programme to provide a further check of the wavelength calibration. The flat-field and sensitivity calibration are discussed in ISR-05-02 (Walsh & Pirzkal 2005) which together with the present ISR is intended to constitute the final documentation of the G800L/WFC grism calibrations.

Data

Following the standard practice for slitless spectroscopy observations, the data were obtained as sets of exposures consisting of one direct image (generally through the F775W filter) and spectroscopic exposures through the G800L grism. A log of all the calibration exposures used here is given in Table 1. During the INTERIM programme, the F775W and G800L images of WR96 were exposed for 1s and 20 s, respectively. For the Cycle 12 WR96 data the exposure times were 1s and 15s. The coverage of the ACS WFC field is illustrated in Figure 1, which shows the different locations of WR96 within the WFC field for the INTERIM (triangles) and Cycle 12 (squares) data. With the new data we approximately double the number of sampling points across both detectors, allowing for an improved mapping of the spatial variations.

The planetary nebula (LMC-SMP-81) was only observed at three locations, two on Chip1 and one on Chip2. For this fainter target, longer exposures were used both for the direct image (30 s) and for the G800L exposures (4 x 200 s). Due to the limited spatial coverage, we do not use these data in the derivation of the wavelength solutions, but they allow an independent verification of the wavelength scale.

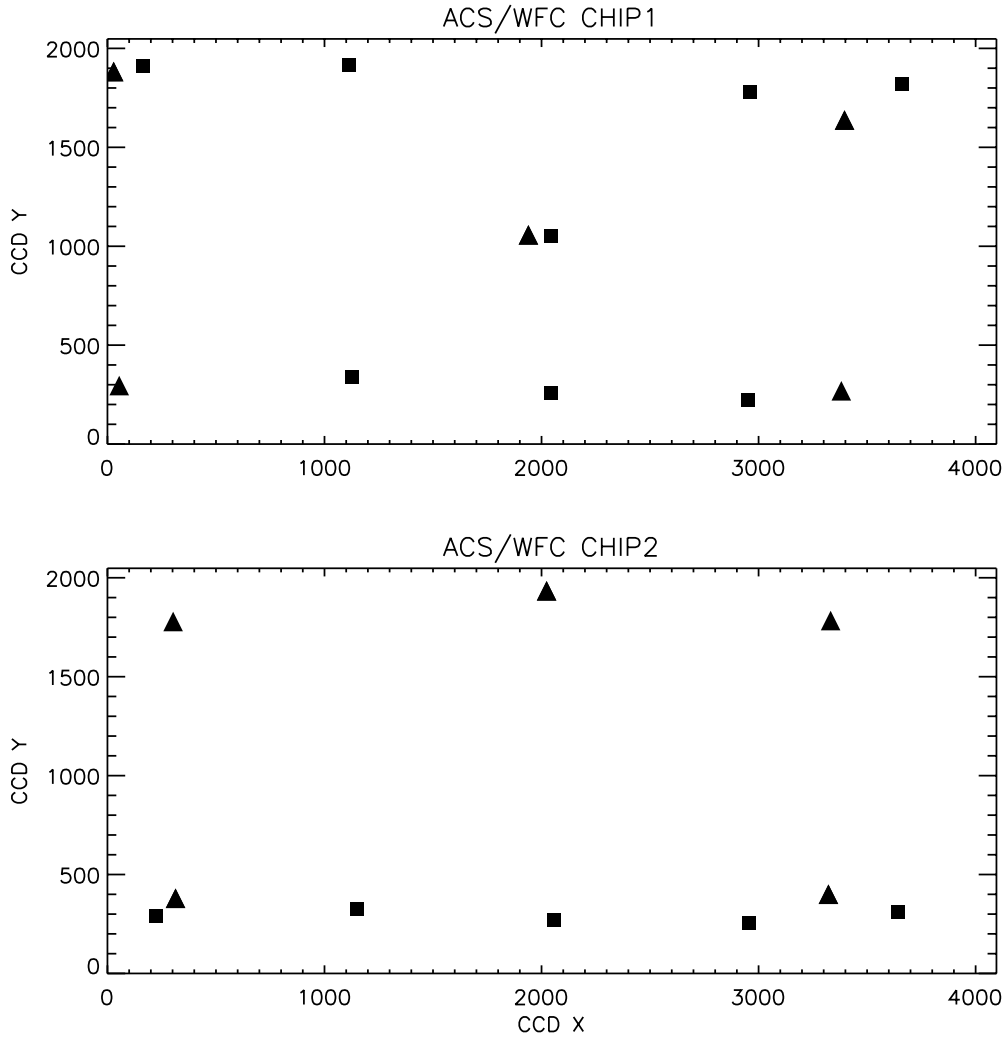

Figure 1: *Coverage of the two ACS/WFC chips by the INTERIM (triangles) and Cycle 12 (squares) data for the Wolf-Rayet star WR96.*

Table 1. Log of calibration exposures.

Filename	Target	Filter	Exptime (s)	POSTARG1 (arcsec)	POSTARG2 (arcsec)
INTERIM					
j8eu06slq	WR96	F775W	1	-91.16	30.38
j8eu06smq	WR96	G800L	20	-91.16	30.38
j8eu06snq	WR96	F775W	1	-91.16	30.38
j8eu06soq	WR96	G800L	20	-91.16	30.38
j8eu06sqq	WR96	F775W	1	-91.16	-45.50
j8eu06srq	WR96	G800L	20	-91.16	-45.50
j8eu06ssq	WR96	F775W	1	0.00	0.00
j8eu06stq	WR96	G800L	20	0.00	0.00
j8eu06suq	WR96	F775W	1	0.00	0.00
j8eu06svq	WR96	G800L	20	0.00	0.00
j8eu07q5q	WR96	F775W	1	-83.66	34.00
j8eu07q6q	WR96	G800L	20	-83.66	34.00
j8eu07q7q	WR96	F775W	1	-83.66	-35.43
j8eu07q8q	WR96	G800L	20	-83.66	-35.43
j8eu07q9q	WR96	F775W	1	-83.66	-35.43
j8eu07qaq	WR96	G800L	20	-83.66	-35.43
j8eu07qbq	WR96	F775W	1	0.15	48.41
j8eu07qcq	WR96	G800L	20	0.15	48.41
j8eu07qdq	WR96	F775W	1	0.15	48.41
j8eu07qeq	WR96	G800L	20	0.15	48.41
j8eua6sxq	WR96	F775W	1	71.66	34.07
j8eua6syq	WR96	G800L	20	71.66	34.07
j8eua6szq	WR96	F775W	1	71.66	34.07
j8eua6t0q	WR96	G800L	20	71.66	34.07
j8eua6t3q	WR96	F775W	1	71.66	-33.02
j8eua6t4q	WR96	G800L	20	71.66	-33.02
j8eua7qlq	WR96	F775W	1	64.68	45.36
j8eua7qmq	WR96	G800L	20	64.68	45.36
j8eua7qnq	WR96	F775W	1	64.68	-24.62

Filename	Target	Filter	Exptime (s)	POSTARG1 (arcsec)	POSTARG2 (arcsec)
j8eua7qoq	WR96	G800L	20	64.68	-24.62
j8eua7qpq	WR96	F775W	1	64.68	-24.62
j8eua7qqq	WR96	G800L	20	64.68	-24.62
Cycle 12					
j8uz01mvq	WR96	F775W	1	0.00	0.00
j8uz01mwq	WR96	G800L	15	0.00	0.00
8uz01myq	WR96	G800L	15	0.00	0.00
j8uz01n1q	WR96	F775W	1	0.00	-39.00
j8uz01n2q	WR96	G800L	15	0.00	-39.00
j8uz01n3q	WR96	F775W	1	-45.00	-39.00
j8uz01n4q	WR96	G800L	15	-45.00	-39.00
j8uz01n5q	WR96	F775W	1	-45.00	37.00
j8uz01n6q	WR96	F606W	180	-45.00	37.00
j8uz01n8q	WR96	G800L	15	-45.00	37.00
j8uz01n9q	WR96	F775W	1	-90.00	32.00
j8uz01naq	WR96	F606W	180	-90.00	32.00
j8uz01ncq	WR96	G800L	15	-90.00	32.00
j8uza1ndq	WR96	F775W	1	45.00	39.00
j8uza1neq	WR96	G800L	15	45.00	39.00
j8uza1nfq	WR96	F775W	1	80.00	44.00
j8uza1ngq	WR96	F606W	180	80.00	44.00
j8uza1niq	WR96	G800L	15	80.00	44.00
j8uza1njq	WR96	F775W	1	45.00	-37.00
j8uza1nkq	WR96	G800L	15	45.00	-37.00
j8uzb1nlq	WR96	F775W	1	0.00	-39.00
j8uzb1nmq	WR96	G800L	15	0.00	-39.00
j8uzb1noq	WR96	F775W	1	-45.00	-39.00
j8uzb1npq	WR96	F606W	180	-45.00	-39.00
j8uzb1nqq	WR96	G800L	15	-45.00	-39.00
j8uzb1ntq	WR96	F775W	1	-90.00	-44.00
j8uzb1nuq	WR96	F606W	180	-90.00	-44.00
j8uzb1nvq	WR96	G800L	15	-90.00	-44.00

Filename	Target	Filter	Exptime (s)	POSTARG1 (arcsec)	POSTARG2 (arcsec)
j8uzc1nxq	WR96	F775W	1	45.00	-37.00
j8uzc1nyq	WR96	F606W	180	45.00	-37.00
j8uzc1nzq	WR96	G800L	15	45.00	-37.00
j8uzc1o1q	WR96	F775W	1	80.00	-32.00
j8uzc1o2q	WR96	F606W	180	80.00	-32.00
j8uzc1o3q	WR96	G800L	15	80.00	-32.00
j8uz02w2q	LMC-SMP-81	F775W	30	0.00	-37.00
j8uz02w3q	LMC-SMP-81	F625W	15	0.00	-37.00
j8uz02w4q	LMC-SMP-81	F625W	15	0.00	-37.00
j8uz02w5q	LMC-SMP-81	F606W	180	0.00	-37.00
j8uz02w6q	LMC-SMP-81	G800L	200	0.00	-37.00
j8uz02w8q	LMC-SMP-81	G800L	200	0.00	-37.00
j8uz02w9q	LMC-SMP-81	G800L	200	0.00	-37.00
j8uz02waq	LMC-SMP-81	G800L	200	0.00	-37.00
j8uz02wjq	LMC-SMP-81	F775W	30	-90.00	31.00
j8uz02wkq	LMC-SMP-81	F606W	180	-90.00	31.00
j8uz02wlq	LMC-SMP-81	G800L	200	-90.00	31.00
j8uz02woq	LMC-SMP-81	G800L	200	-90.00	31.00
j8uz02wqq	LMC-SMP-81	G800L	200	-90.00	31.00
j8uz02wrq	LMC-SMP-81	G800L	200	-90.00	31.00
j8uza2xtq	LMC-SMP-81	F775W	30	80.00	-31.00
j8uza2xuq	LMC-SMP-81	F606W	180	80.00	-31.00
j8uza2xwq	LMC-SMP-81	G800L	200	80.00	-31.00
j8uza2y0q	LMC-SMP-81	G800L	200	80.00	-31.00
j8uza2y1q	LMC-SMP-81	G800L	200	80.00	-31.00
j8uza2y2q	LMC-SMP-81	G800L	200	80.00	-31.00

Analysis

The raw data were downloaded from the ST-ECF archive and initial processing was done with the CALACS task in STSDAS in IRAF. In order to save bandwidth during the observations, only a 4096 x 400 pixels sub-window of the full CCD detectors was read out.

Prior to further analysis, the sub-windowed exposures were copied into full-size (4096x2048 pixels) images at the proper locations, using the CENTERA1, CENTERA2, SIZAXIS1 and SIZAXIS2 header keywords. Throughout this report, all analysis is done on these non-drizzled ('flt') files and all trace- and wavelength solutions are given with respect to non-drizzled images. Since parameters such as image scale and orientation will change during drizzling (e.g. the default behavior of Multidrizzle is to drizzle images with North up) it is not possible to give general calibration relations that would apply to any given set of drizzled images. However, users who wish to apply the drizzle algorithm to ACS slitless spectroscopy should note that aXe versions 1.4 and later have a set of tasks designed specifically for this purpose, which use the trace and wavelength solutions as defined in this document. We are ignoring the effects of differential velocity aberration (Cox & Gilliland 2002). While this effect can lead to corner-to-corner stretches in the image scale of about 1.5 pixels for exposures taken 6 months apart, all calibrations discussed here are defined with respect to object coordinates in a reference exposure which is generally assumed to be taken immediately before the grism exposure. Over the course of 1 orbit, differential velocity aberration will lead to a maximum shift of about 0.1 pixels in the wavelength (x-) direction, or about 5 Å at most. Users who are extracting slitless spectra based on object catalogues from other sources, or taken at different epochs than the grism exposures, may need to consider the effect of differential velocity aberration, however.

Figure 2 shows one of the G800L grism exposures of WR96 with the locations of the various orders indicated on the figure. Spectra of several fainter sources in the field are also visible.

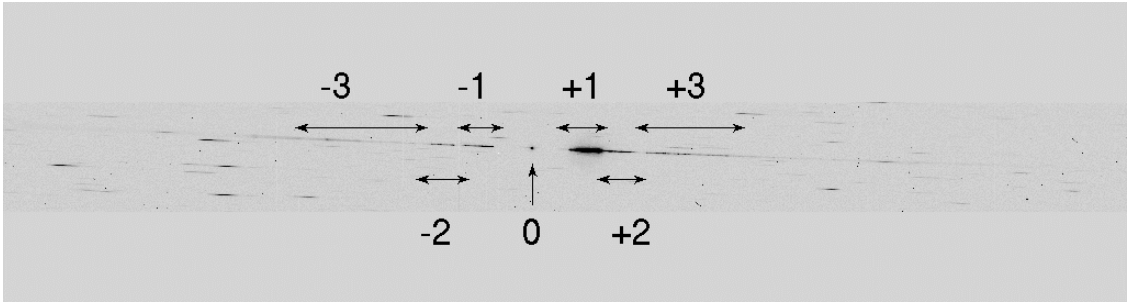

Figure 2: A G800L grism spectrum of the Wolf-Rayet star WR-96. The approximate locations of the -3...+3 orders are indicated.

The locations of spectral traces and wavelength solutions for the G800L exposures were defined with respect to the position of the object in the corresponding direct images. The position of WR96 was located by running SExtractor on each of the F775W images and removing other objects from the resulting SExtractor catalogues.

Tracing the orders

The individual spectral orders were traced by measuring the centroid across the spectra on the G800L exposures as a function of offset $\Delta X = X\text{-}X_{ref}$ in the CCD X-direction with respect to the object position (X_{ref},Y_{ref}) in the corresponding direct image. We found the traces to be well approximated by linear fits with the coefficients given in Table 2, with an r.m.s. scatter of well below 0.1 pixels around the fit for the 1st order and up to ~0.5 pixels for the -3rd order. The trace definitions are of the form $(Y\text{-}Y_{ref}) = DYDX\_0 + DYDX\_1 * \Delta X$, where the DYDX_0 and DYDX_1 terms are field dependent and given in the usual format used by the ST-ECF aXe reduction package, e.g.: $DYDX\_1 = a0 + a1 * X_{ref} + a2 * Y_{ref} + a3 * X_{ref}^2 + ...$ (see the aXe manual for details). For the 0th order we have simply adopted the first-order trace description.

The trace descriptions derived here are quite similar to those of Pasquali et al. (2003a). In particular, we find a similar tilt of the spectra of about -2 degrees on average with respect to the CCD X-axis. Within the uncertainties on the fits, most of the traces pass within 1 pixel of the reference point. We also carried out the fits separately for the INTERIM and Cycle 12 datasets, but found no discernible differences. The values in Table 2 are based on the combined data. For many of the higher order coefficients, the uncertainties are actually larger than the fitted values themselves, but we have included 2nd order terms in the surface fits for all terms nonetheless as we found this to result in slightly better agreement with the previous solutions by Pasquali et al. (2003a).

The uncertainties on the fits are comparable to or smaller than the typical accuracy by which the centroids of faint objects can be determined in the direct images, and we do not expect that the current trace descriptions will generally be a limiting factor for tracing the spectra.

Table 2. Spectral trace definitions. Numbers in parantheses denote uncertainties on the fitted coefficients.

Term	**a0**	**a1(X)**	**a2(Y)**	**a3(X^2)**	**a4(XY)**	**a5(Y^2)**
CHIP1‘						
+1st order	-30..160 pixels					
DYDX_A_0	-0.78 (0.08)	-1.32E-5 (6.23E-5)	-2.79E-4 (1.71E-4)	1.35E-8 (1.65E-8)	1.516E-7 (1.96E-8)	-2.88E-9 (7.56E-8)

Term	a0	a1(X)	a2(Y)	a3(X^2)	a4(XY)	a5(Y^2)
DYDX_A_1	-0.0345 (0.0007)	2.100E-6 (5.01E-7)	-5.42E-6 (1.37E-6)	-2.0E-10 (1.3E-10)	2.75E-10 (1.57E-10)	1.92E-10 (6.08E-10)
+2nd order	120..410 pixels					
DYDX_C_0	-0.17 (0.32)	-1.29E-4 (2.49E-4)	-8.26E-4 (6.80E-4)	3.01E-8 (6.59E-8)	2.40E-7 (7.80E-8)	1.52E-7 (3.01E-7)
DYDX_C_1	-0.0385 (0.0015)	1.79E-6 (1.19E-6)	-3.08E-6 (3.26E-6)	-1.20E-10 (3.16E-10)	5.79E-11 (3.73E-10)	-8.7E-10 (1.44E-9)
+3rd order	260..660 pixels					
DYDX_D_0	-1.17 (0.26)	-4.87E-4 (2.05E-4)	3.13E-4 (5.62E-4)	1.65E-7 (5.44E-8)	1.78E-7 (6.44E-8)	-4.35E-7 (2.49E-7)
DYDX_D_1	-0.0355 (7.3E-4)	2.52E-6 (5.72E-7)	-6.12E-6 (1.56E-6)	-4.20E-10 (1.52E-10)	2.63E-10 (1.79E-10)	6.41E-10 (6.93E-10)
-1st order	-390..-220 pix.					
DYDX_E_0	0.56 (2.70)	-0.0045 (0.0029)	0.0048 (0.0034)	1.12E-6 (7.10E-7)	-5.21E-7 (6.38E-7)	-1.97E-6 (1.30E-6)
DYDX_E_1	-0.0327 (0.010)	-1.43E-5 (1.06E-5)	1.21E-5 (1.26E-5)	3.76E-9 (2.62E-9)	-1.95E-9 (2.36E-9)	-7.43E-9 (4.80E-9)
-2nd order	-540..-300 pix					
DYDX_F_0	2.54 (1.61)	-0.0030 (0.0016)	4.77E-4 (0.0018)	7.45E-7 (3.47E-7)	-4.85E-7 (2.72E-7)	-6.08E-8 (7.14E-7)
DYDX_F_1	-0.0308 (0.0034)	-4.63E-6 (3.38E-6)	-3.77E-6 (3.78E-6)	1.45E-9 (7.49E-10)	-1.13E-9 (5.87E-10)	-7.20E-10 (1.54E-9)
-3rd order	-980..-450 pix					
DYDX_G_0	-0.84 (1.62)	0.0011 (0.0016)	-0.0050 (0.0018)	-4.35E-7 (3.50E-7)	4.66E-7 (2.74E-7)	1.84E-6 (7.20E-7)
DYDX_G_1	-0.038 (0.002)	3.50E-6 (2.25E-6)	-1.25E-5 (2.51E-6)	-8.20E-10 (4.98E-10)	8.35E-10 (3.90E-10)	2.08E-9 (1.03E-9)
CHIP2						
+1st order	-30..160 pixels					
DYDX_A_0	0.25 (0.46)	-4.55E-4 (2.19E-4)	-6.62E-4 (0.0013)	2.97E-8 (5.66E-8)	1.96E-7 (5.74E-8)	1.15E-7 (6.13E-7)
DYDX_A_1	-0.025 (0.001)	1.04E-6 (6.77E-7)	-6.09E-6 (4.12E-6)	-1.40E-10 (1.75E-10)	-6.20E-11 (1.77E-10)	1.09E-9 (1.89E-9)
+2nd order	120..410 pix					
DYDX_C_0	1.19 (0.37)	-6.38E-4 (1.76E-4)	-0.0029 (0.0011)	9.73E-8 (4.55E-8)	1.85E-7 (4.62E-8)	1.13E-6 (4.93E-7)
DYDX_C_1	-0.0297 (0.0022)	2.20E-6 (1.05E-6)	6.65E-6 (6.36E-6)	-5.70E-10 (2.70E-10)	1.42E-10 (2.74E-10)	-5.16E-9 (2.92E-9)
+3rd order	260..660 pixels					

Term	a0	a1(X)	a2(Y)	a3(X^2)	a4(XY)	a5(Y^2)
DYDX_D_0	0.42 (0.96)	-3.73E-4 (4.63E-4)	-5.16E-4 (0.0028)	2.05E-8 (1.19E-7)	1.20E-7 (1.21E-7)	1.09E-7 (1.29E-6)
DYDX_D_1	-0.0261 (0.0013)	9.00E-7 (6.21E-7)	-3.64E-6 (3.78E-6)	-2.10E-10 (1.60E-10)	3.29E-10 (1.63E-10)	-6.60E-10 (1.74E-9)
-1st order	-390..220 pix					
DYDX_E_0	2.47 (1.20)	-0.0019 (5.5E-4)	-0.0050 90.0032)	3.73E-7 (1.33E-7)	2.79E-7 (1.17E-7)	1.98E-6 (1.44E-6)
DYDX_E_1	-0.0162 (0.0035)	-3.70E-6 (1.63E-6)	-1.96E-5 (9.45E-6)	8.72E-10 93.94E-10)	4.07E-10 (3.48E-10)	5.59E-9 (4.26E-9)
-2nd order	-540..-300 pix					
DYDX_F_0	2.92 (2.87)	-7.01E-4 (0.0018)	-0.0064 (0.0062)	6.71E-8 (3.77E-7)	6.38E-7 (3.99E-7)	1.96E-6 (2.58E-6)
DYDX_F_1	-0.0186 (0.0045)	1.38E-6 (2.78E-6)	-1.56E-5 (9.64E-6)	-3.10E-10 (5.87E-10)	9.85E-10 (6.22E-10)	2.60E-9 (4.02E-9)
-3rd order	-980..-450 pix					
DYDX_G_0	-2.40 (0.22)	8.58E-4 (1.35E-4)	0.0055 (4.68E-4)	-1.77E-7 (2.86E-8)	-3.33E-7 (3.02E-8)	-2.32E-6 (1.95E-7)
DYDX_G_1	-0.0274 (0.0012)	3.46E-6 (7.50E-7)	5.08E-6 (2.60E-6)	-6.00E-10 (1.58E-10)	-8.50E-10 (1.68E-10)	-4.58E-9 (1.08E-9)

Wavelength solutions

The trace definitions in Table 2 were inserted into configuration files for the aXe software and each spectral order was extracted using a 10 pixels wide (+/-5 pixels around the trace) extraction box. For this initial extraction the aXe configuration file was defined in such a way that the wavelength scale of the extracted spectra was identical to the trace distance. For the actual wavelength calibration we adopted a somewhat different approach than in Pasquali et al. (2003a), where the wavelength solutions were derived by directly measuring the Δ X location along the trace of several features in the observed spectra and carrying out polynomial fits to wavelength vs. Δ X. Instead, we carried out a direct least-squares fit of the G800L spectra to a (smoothed) spectrum of WR96 obtained from the ground (Pasquali et al. 2001). This approach has the advantage that blends are automatically accounted for, and thus does not rely on the ability to accurately measure the wavelengths of individual spectral features.

The wavelength solutions were assumed to be of the form Lambda(ΔX) = DLDP_0 + DLDP_1 * ΔX (+ DLDP_2 * ΔX^2), with the DLDP_* terms being field-dependent in the usual aXe way, as for the trace descriptions. We did not include the second-order term for all orders, hence the paranthesis. For each observation, we solved for the minimum r.m.s.

difference between the G800L spectrum and the ground-based reference spectrum as a function of DLDP_* and a smoothing length applied to the ground-based spectrum. We experimented with various smoothing functions and found a standard Gaussian function to provide adequate results. Since the grism spectra were not flux calibrated at this stage, the reference spectrum was also multiplied by a 4th-order polynomial fit to the ratio of the two spectra before the r.m.s. difference was calculated. We preferred this approach, rather than attempting to flux calibrate the G800L spectra, since this would cause the low-sensitivity regions of the spectra near the end of the wavelength range to be weighted too strongly. The actual fitting was implemented as an IDL program, using the AMOEBA minimization routine (Press et al. 1992).

Figure 3 shows the best fit between the smoothed and scaled ground-based spectrum of WR96 and one of the 1st-order G800L spectra. Evidently, the fit is not perfect. While the differences may be partly caused by spectral variability of the star we did not find any large changes in the spectra between the INTERIM and Cycle 12 datasets. On the other hand, some of the differences (e.g. around 7600 Å) appear too systematic to be accounted for simply by inapproppriate smoothing and/or errors in the wavelength solution and we have not been able to achieve a better fit by changing the smoothing function. One potential worry is that this spectral mismatch might lead to systematic errors in the wavelength solutions (e.g. if the relative strengths of blended lines change). It is difficult to assess the errors introduced by such effects, but from Figure 3 the locations of major features in the spectrum are fairly well reproduced. As discussed below, the planetary nebula observations provide an independent consistency check.

Each of the DLDP* coefficients were fitted with two-dimensional polynomials as function of (X_{ref},Y_{ref}) position in order to provide a smooth representation of the variation across the field. The resulting wavelength solution coefficients are given in Table 3. For the +1st and +2nd orders, for which an accurate wavelength calibration is most likely to be desirable and where the higher S/N allows a more accurate determination of the wavelength solution, the wavelength solutions are given as 2nd-order polynomials. For these orders the field dependence also includes 2nd-order terms in X and Y position. For the remaining orders we only give 1st-order (linear) wavelength solutions and spatial terms. For completeness, we have also included the terms for the 0th order spectrum, copied from the INTERIM calibration. The last column in the table gives the r.m.s. deviation around the 2-d polynomial fit for each coefficient. Note that the wavelength range used to derive the wavelength calibration varies somewhat for the different orders, due to the different sensitivity curves of each order and overlap between the orders. In particular, the sensitivity of the +/-2nd orders drops rapidly beyond about 7000 Å.

As for the trace definitions, we carried out separate fits for the INTERIM and Cycle 12 data and found no significant changes in the wavelength solutions, although the comparison is somewhat limited by the different spatial coverage of the two epochs. The performance of the G800L appears to be stable within the accuracy that we can measure (better than 1 pixel). The coefficients in Table 3 are based on the combined data and utilizes the full spatial coverage of both datasets as illustrated in Figure 1.

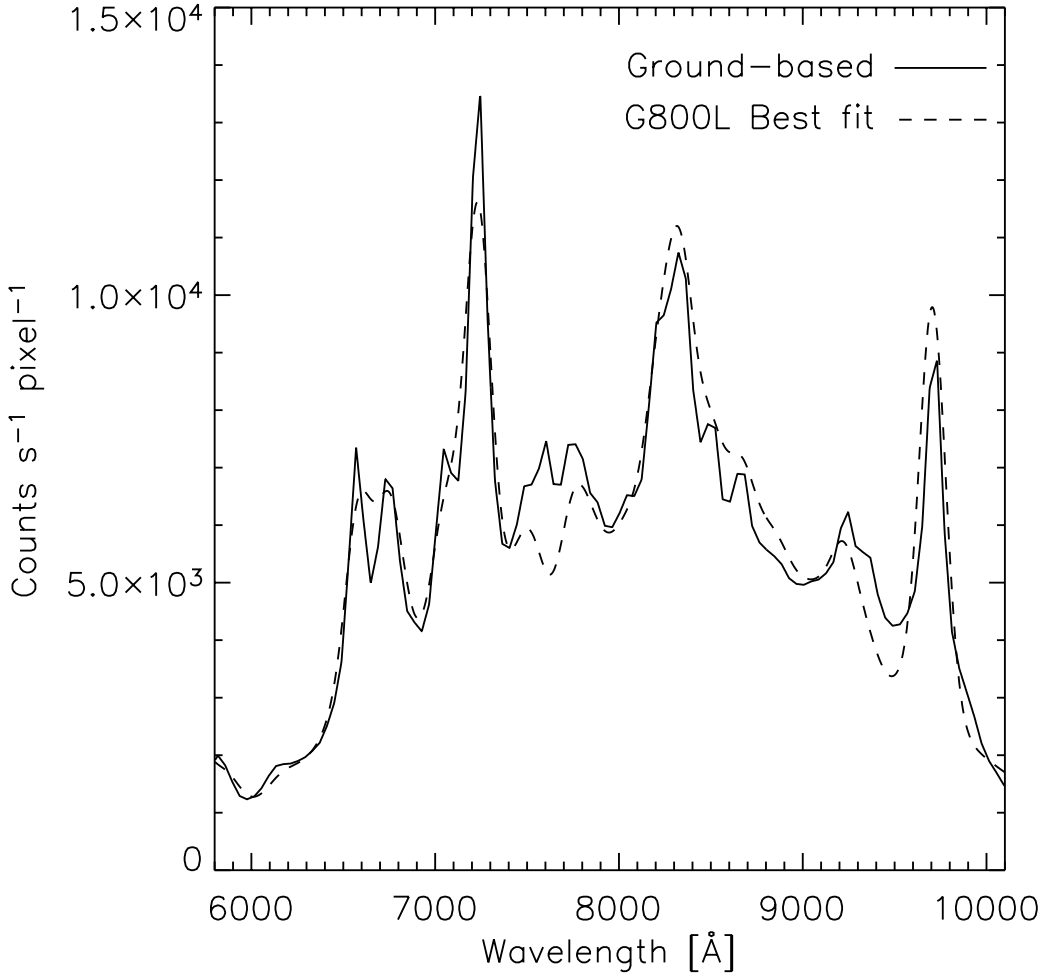

Figure 3: Smoothed ground-based spectrum of WR96 and the best-fitting G800L spectrum.

Table 3. Wavelength solution coefficients for the ACS/WFC G800L. The +1st, +2nd, +3rd, 0th, -1st, -2nd and -3rd orders are represented by the terms DLDP_A_*, DLDP_C_*, DLDP_D_*, DLDP_B_*, DLDP_E_*, DLDP_F_* and DLDP_G_*. Each term is field dependent and is given as e.g. DLDP_A_0 = a0 + a1*X + a2*Y + ...

Term	a0	a1 (X)	a2 (Y)	a3 (X^2)	a4 (XY)	a5 (Y^2)	r.m.s.
CHIP1							
+1st order,	5800-10100 Å						
DLDP_A_0	4787.3	0.003893	-0.07142	-8.06E-7	5.226E-7	3.040E-5	9.90
DLDP_A_1	37.3017	0.00184	-2.12E-4	-1.14E-7	-7.94E-8	-3.94E-7	0.24
DLDP_A_2	0.005756	-1.88E-6	-4.89E-6	7.21E-10	-1.9E-10	2.159E-9	0.0013
+2nd order	5400-7400 Å						
DLDP_C_0	2654.0	0.064507	-0.10756	-1.68E-5	1.112E-5	2.197E-5	22.9
DLDP_C_1	16.8471	1.064E-4	4.145E-4	1.482E-7	-1.34E-7	-1.54E-7	0.26
DLDP_C_2	0.00608	1.839E-6	-2.89E-6	-3.7E-10	1.70E-10	5.40E-10	0.0007
+3rd order	6500-8000 Å						
DLDP_D_0	1539.7	0.001748	0.00532				12.1
DLDP_D_1	13.2208	4.611E-4	-4.47E-4				0.04
0th order	-						
DLDP_B_0	86700	-3.06904	2.41291				
DLDP_B_1	650.0						
-1st order	5500-8500 Å						
DLDP_E_0	-5030.4	-0.02779	0.025159				33.1
DLDP_E_1	-39.1881	-0.00167	0.001443				0.14
-2nd order	5500-7500 Å						
DLDP_F_0	-2323.5	-0.01288	0.002881				17.50
DLDP_F_1	-18.877	-7.99E-4	6.625E-4				0.045
-3rd order	5500-9000 Å						
DLDP_G_0	-1425.3	-0.04657	0.042361				58.1
DLDP_G_1	-12.3046	-5.86E-4	4.954E-4				0.07
CHIP2							
+1st order,	5800-10100 Å						
DLDP_A_0	4750.5	0.034373	0.054715	-9.56E-6	-2.03E-6	-2.88E-5	5.2
DLDP_A_1	40.6661	0.001464	-0.00364	6.854E-8	-9.22E-8	1.205E-6	0.17
DLDP_A_2	4.618E-4	1.499E-6	1.783E-5	-3.8E-10	4.11E-11	-8.96E-9	0.001

Term	a0	a1 (X)	a2 (Y)	a3 (X^2)	a4 (XY)	a5 (Y^2)	r.m.s.
+2nd order	5400-7400 Å						
DLDP_C_0	2656.4	0.046017	-0.15926	-2.47E-6	-4.20E-6	7.407E-5	20.5
DLDP_C_1	17.8244	4.398E-4	0.001314	-2.62E-8	1.069E-8	-8.78E-7	0.25
DLDP_C_2	0.00739	1.231E-6	-6.37E-6	1.49E-10	-2.5E-10	2.863E-9	0.0007
+3rd order	6500-8000 Å						
DLDP_D_0	1521.5	0.013904	-0.01782				38.7
DLDP_D_1	14.0995	5.193E-4	-4.47E-4				0.11
0th order	-						
DLDP_B_0	81285.0	-2.84255	2.33561				
DLDP_B_1	650.0						
-1st order	5500-8500 Å						
DLDP_E_0	-5003.6	-0.05192	0.03047				55.5
DLDP_E_1	-41.4899	-0.00206	0.001624				0.27
-2nd order	5500-7500 Å						
DLDP_F_0	-2361.9	-0.01807	0.025267				55.0
DLDP_F_1	-20.1381	-9.52E-4	7.919E-4				0.14
-3rd order	5500-9000 Å						
DLDP_G_0	-1403.8	-0.04733	-0.00197				72.9
DLDP_G_1	-13.049	6.82E-4	4.791E-4				0.12

Comparison with the Previous Calibration

In Figure 4 and Figure 5 we show the difference between the new wavelength calibration for the +1st order and that of Pasquali et al. (2003a) for the two chips. Each figure shows the difference between the two calibrations (in Å) as a function of wavelength for 15 positions across the detector. The difference is generally less than about 1 pixel, except near the lower right-hand corner of Chip 1 where the offset reaches some 70 Å (1.8 pixels). These relatively minor differences are likely due to a combination of our improved spatial coverage and the different fitting technique used here. Especially at off-center locations, the present calibration is expected to constitute an improvement compared to Pasquali et al. (2003a).

Although the old and new wavelength calibrations are very similar over most of the field, the slight changes do have some effect on the sensitivity calibration as well. Over most of the wavelength range (5800Å - 9000Å) the change in the flux calibration amounts to less than 3%, but at 10500Å the difference can be as large as 5%-8%. We will release updated sensitivity files for aXe to reflect these changes.

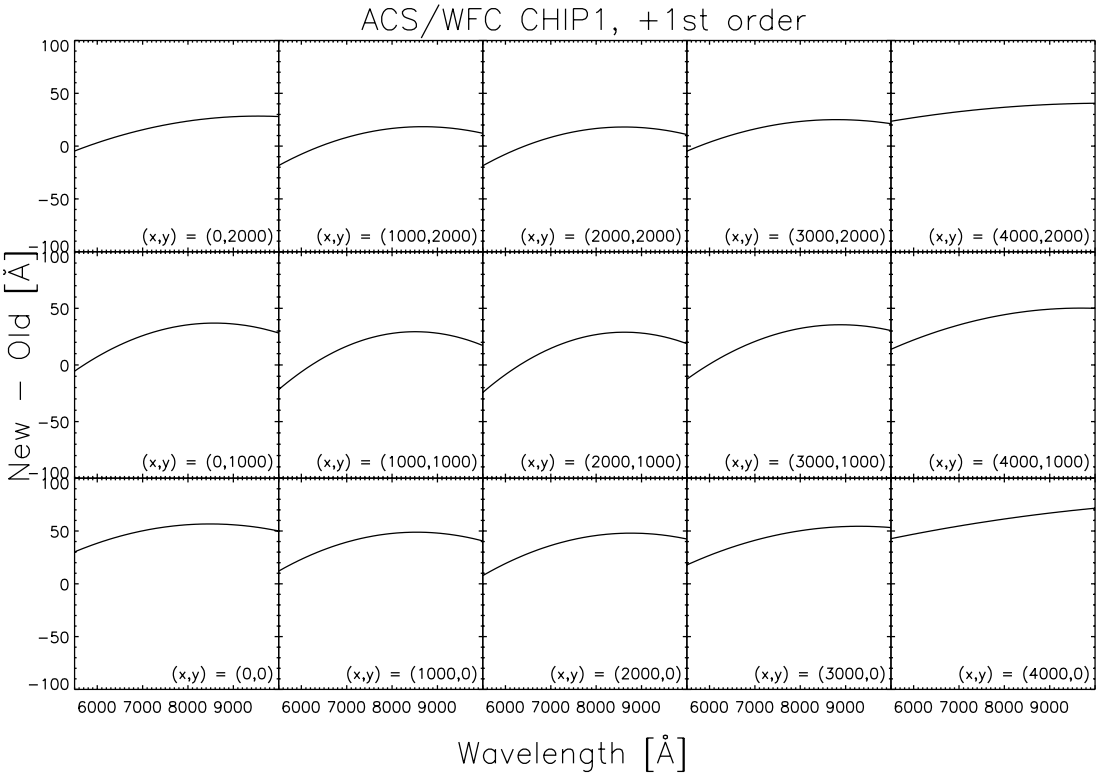

Figure 4: Difference between the Pasquali et al. (2003a) and our wavelength calibration for the WFC/G800L 1st-order spectra (Chip1).

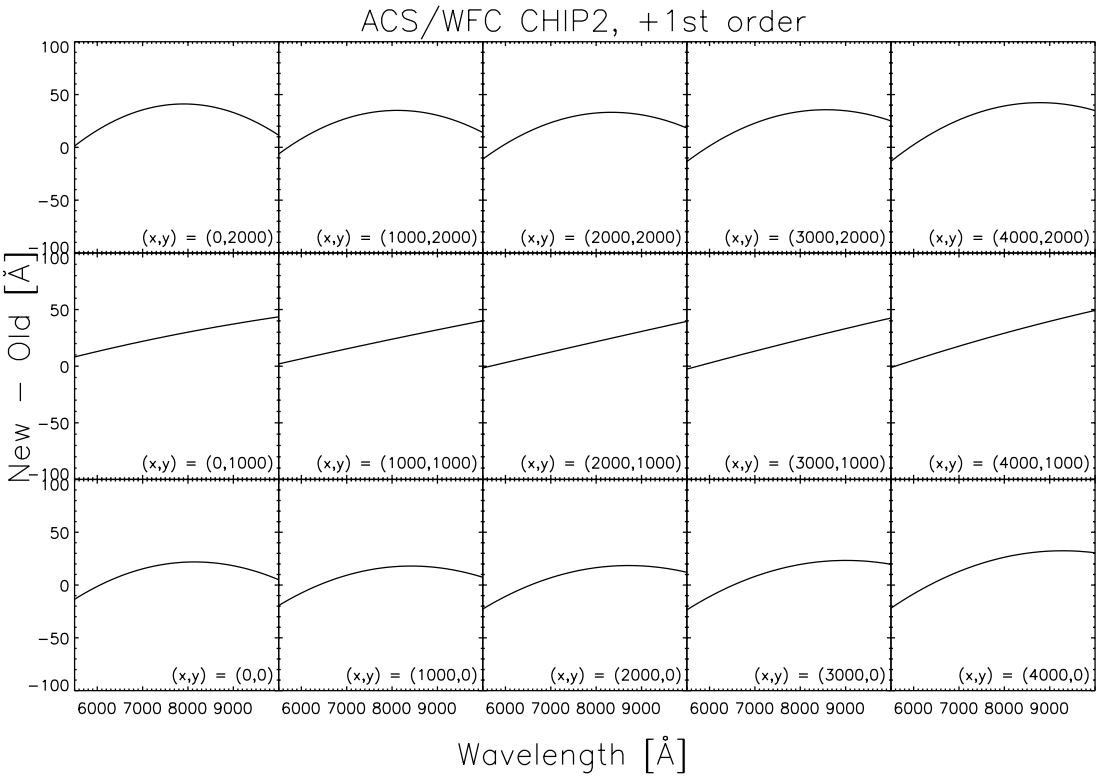

Figure 5: Same as Figure 4, but for Chip 2.

Comparison with the LMC-SMP-81 spectra

As a further check of the wavelength calibration, spectra of LMC-SMP-81 were extracted with aXe. The resulting spectrum is shown in Figure 6, where some prominent features are also labeled. By measuring the centroids of the various features and comparing with their expected wavelengths (correcting for an LMC radial velocity of 270 km/s) we generally find agreement within a maximum absolute difference of about 30 Å, except for the datasets j8uza2xwq-j8uza2y2q (CHIP 2) where the measured wavelength of the [Ar III] 7135 Å line is too short by about 40 Å. An exact match is anyway not expected, since many of the features seen in the grism spectrum are blends of several lines (Halpha is blended with [N II] at 6583 Å, and the [O II] “line” at about 7325 Å actually consists of 4 individual lines between 7319 Å and 7330 Å). However, the comparison with the spectra of LMC-SMP-81 again suggests that the wavelength calibration is accurate to better than 1 pixel.

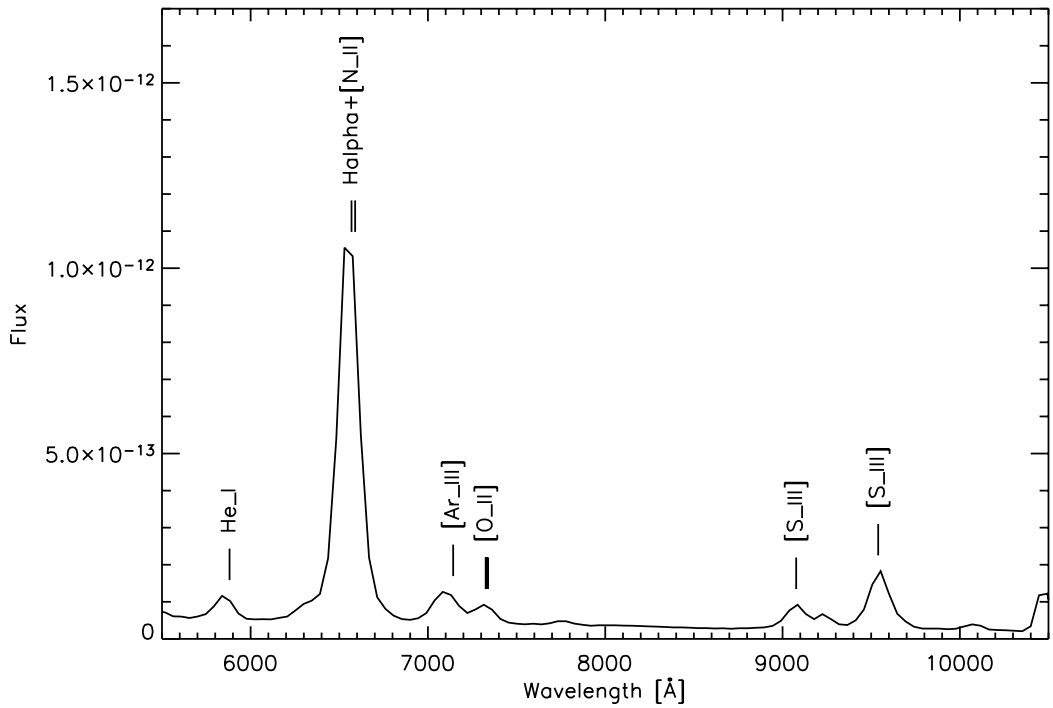

Figure 6: aXe extracted spectrum of LMC-SMP-81. Some features are marked.

Summary

An updated wavelength calibration of the G800L grism for the ACS Wide Field Camera has been presented. The new calibration is found to be in agreement with the previous one within 1 pixel over nearly the entire ACS/WFC field of view. We have implemented the revised calibration in new configuration files for the aXe spectral extraction software, available via the ST-ECF web site. Although the difference between the old and new calibration is minor, it is recommended that future reductions of ACS G800L slitless spectroscopy data make use of the revised calibration, which includes more data and has better spatial coverage across both chips.

Acknowledgements

We thank H. Kuntschner, K. Sembach, R. Gilliland and R. Bohlin for a number of useful comments and suggestions which helped improve this report.

References

Cox, C., & Gilliland, R., 2002, *The Effect of Velocity Aberration on ACS Image Processing*, HST Calibration Workshop, STScI
Pasquali, A., Pirzkal, N., Walsh, J. R., 2001, *Selection of Wavelength Calibration Targets for the ACS Grism*, ISR ACS 2001-004
Pasquali, A., Pirzkal, N., Walsh, J. R., 2003a, *The in-orbit Wavelength Calibration of the WFC G800L Grism*, ISR ACS 2003-001
Pasquali, A., Pirzkal, N., Walsh, J. R., 2003b, *The in-orbit Wavelength Calibration of the HRC G800L grism*, ISR ACS 2003-007
Press, W. H., Teukolsky, S. A., Vetterling, W. T. & Flannery, B. P., 1992, *Numerical Recipes in Fortran*, Cambridge University Press
Walsh, J. R., Pirzkal, N., 2005. *Flat-Field and Sensitivity Calibration for ACS G800L slitless spectroscopy modes*. ISR ACS 2005-002.